

Amplification and stability of magnetic fields and dynamo effect in young A stars

R. Arlt* and G. Rüdiger

Astrophysikalisches Institut Potsdam, An der Sternwarte 16, D-14482 Potsdam, Germany

Accepted Received . . . ; in original form . . .

ABSTRACT

This study is concerned with the early evolution of magnetic fields and differential rotation of intermediate-mass stars which may evolve into Ap stars. We report on simulations of the interplay of differential rotation and magnetic fields, the stability limits and non-linear evolution of such configurations, and the prospects of dynamo action from the unstable cases. The axisymmetric problem delivers a balance between field amplification and back-reaction of the magnetic field on the differential rotation. The non-axisymmetric case involves also the Tayler instability of the amplified toroidal fields. We consider limits for field amplification and apply these to young A stars.

Apart from its application to Ap stars, the instability is scrutinized for the fundamental possibility of a dynamo. We are not looking for a dynamo as an explanation for the Ap star phenomenon. The kinetic helicity is concentrated near the tangent cylinder of the inner sphere of the computational domain and is negative in the northern hemisphere. This appears to be a ubiquitous effect not special to the Tayler instability. The latter is actually connected with a positive current helicity in the bulk of the spherical shell giving rise to a small, but non-vanishing α -effect in non-linear evolution of the instability.

Key words: MHD – stars: magnetic field – stars: chemically peculiar.

1 INTRODUCTION

Stellar objects involve in many cases the amplification of magnetic fields by differential rotation. The differential rotation at the bottom of the solar convection zone, for example, acts as a generator for toroidal magnetic fields while the differential rotation is imposed from the convection zone. In principle, there is a large domain of radiative zones in stars in which the amplification by differential rotation is conceivable, where no convective motions disturb the winding-up. This concerns the whole range of intermediate-mass and massive stars from 1.2 solar masses up to several tens of a solar mass. All these stars possess large radiative envelopes (apart from a possible, very thin convective surface layer). We will often speak about A and Ap stars in this Paper, but the simulations are actually applicable to a wider range of stars possessing non-convective domains, such as solar-like stars with radiative interiors or more massive B stars.

According to Stepien (2000), the pre-main-sequence evolution of stars with masses near two solar masses is accompanied by changes in angular momentum through disk accretion, magnetic star-disk coupling, and magnetized winds. All these effects likely lead to a differentially rotating interior. When approaching the zero-age main sequence (ZAMS), the stars have established their radiative envelopes, and accretion has ceased. It is then mainly by mag-

netized winds that the angular velocity is reduced. This, however, affects only the surface, while it takes extremely long for the small plasma viscosity to reduce also the angular velocity in the interiors. The coupling of the surface to the interior is strongly enhanced by magnetic fields. There are a few cases for which an increase of the surface rotation period has actually been observed, such as V901 Ori (Mikulašek et al. 2008).

Another source for differential rotation, especially for stars with masses less than $2.5M_{\odot}$, may be the convective phase in the pre-main-sequence evolution. While there is no specific model available for a progenitor of A stars, the computations by Küker & Rüdiger (2008) indicate tendencies of stronger differential rotation for faster rotation, hotter surface temperatures, and especially thinner convective envelopes. To which extent the differential rotation will be present in the remaining radiative star is debatable, since small magnetic fields in the (then) radiative interior are sufficient to prevent differential rotation from spreading below the convection zone (Rüdiger & Kitchatinov 1997; Gough & McIntyre 1998).

Studying the interaction between differential rotation and magnetic fields is important for the understanding of the existence of magnetic Ap stars, and for the explanation why only a fraction of A stars show the peculiarities. Differential rotation or magnetic fields or combinations of the two may become unstable against small perturbations (e.g. Watson 1981; Gilman & Fox 1997; Dikpati et al. 2004; Braithwaite 2006b; Arlt et al. 2007; and many others). Where MHD is a suitable description of the astrophysical

* E-mail: rarlt@aip.de

objects, we can group the instabilities into shear-driven, current-driven, and buoyancy-driven instabilities.

Current-driven instabilities are particularly interesting for toroidal magnetic fields, since these typically reach the largest strengths if differential rotation is present. Such toroidal fields also come along with currents giving rise to a kink-type instability, whose most easily excited modes are typically modes with low azimuthal wave number (Vandakurov 1972; Taylor 1973; Spruit 1999). We refer to this instability here as Taylor instability.

Dynamo action arising from the Taylor instability was suggested heuristically by Spruit (2002) and later in simulations by Braithwaite (2006a) who found sustained, but not constant magnetic field energies in a differentially rotating cylindrical domain. Spherical, three-dimensional simulations of the solar radiative interior have been performed by Brun & Zahn (2006) where the evolution of a fossil field together with an imposed rotation profile at the top of the domain (i.e. the bottom of the convection zone) was investigated. The initial poloidal magnetic field as well as the later combination of toroidal and poloidal fields showed distinct instability signatures. The simulations were examined by Zahn, Brun & Mathis (2007) on possible dynamo action, but none was found. The difference between the two attempts may be the presence of an enforced differential rotation inside the domain of Braithwaite's (2006a) simulations, as opposed to the enforcement on the boundary only in the computations by Zahn et al. (2007). Another non-linear simulation of the Taylor instability was performed by Gellert, Rüdiger & Elstner (2008) who also used a cylindrical setup with a differential rotation enforced at the outer radial boundary, but in this case depending on vertical direction z only. In terms of a dynamo- α they find values of $|\alpha_{zz}| \sim 0.05$ measured against an imposed vertical field. That $|\alpha_{zz}|$ is 100 per cent of the rms velocity implying that the flow is entirely helical. However, all magnetic modes decay when the external magnetic field is switched off.

The precise nature of the non-linear evolution of the Taylor instability with a possible dynamo effect is thus a very interesting issue on which we follow up here. The scenario of amplification of magnetic fields by differential rotation, the stability of the resulting configurations, and the possible dynamo effect in case of instability is very general to non-convective zones in a wide range of stars. Section 2 describes how the computations were set up, while Section 3 shows the results of the axisymmetric, non-linear simulations for the field-amplification. The analysis in Section 4 deals with the stability of the results in Section 3, and Section 5 evolves the full three-dimensional and non-linear problem. Dynamo coefficients are derived in Section 6. With respect to the instability, we will focus on the pre-main-sequence evolution of Ap stars here, whereas the possible dynamo action is not believed to be an important Ap star phenomenon, but is of general interest for dynamo theory.

2 NUMERICAL SETUP

The computational domain is a spherical shell with the radius r running from an inner radius r_i to an outer radius r_o which is normalized to one by the stellar radius R in the following. The colatitude θ always covers the range from 0 to π ; the azimuthal coordinate ϕ runs from 0 to 2π in the non-axisymmetric simulations. The inner radius was set to $r_i = 0.5$ in all the computations of this study.

The investigation involves three steps: Step I one is an axisymmetric simulation with an initial differential rotation $\Omega(s)$ where

$s = r \sin \theta$ is the axis distance, and an initial poloidal magnetic field $\mathbf{B} = (B_r(r, \theta), B_\theta(r, \theta), 0)$.

Step II is a stability analysis where a number of snapshots of the simulation of the first step is used as background states for a linear analysis of the stability of the system against non-axisymmetric perturbations. We will restrict ourselves to the stability of perturbations with azimuthal wave-numbers of $m = 1$.

Step III consists of fully non-linear, three-dimensional computations of the evolution. In these simulations, the non-axisymmetric perturbation is either present from the beginning, or is imposed at a later step as an external 'kick' to the system. We can thus compare the evolutions of states which are either Taylor-stable or Taylor-unstable according to Step II. The non-linear evolutions also allow to assess the possibility of driving a dynamo with the instability. Dynamo effect will be visible only in terms of non-vanishing dynamo-coefficients of a mean-field description, but not in growing and sustained magnetic fields, because our system lacks a source of energy.

The computations employ the spherical MHD code by Hollerbach (2000) which integrates the momentum, induction, and temperature equations in the Boussinesq approximation. We are not using temperature fluctuations in this study; the normalized, incompressible MHD equations are thus

$$\frac{\partial \mathbf{u}}{\partial t} = -(\mathbf{u} \cdot \nabla) \mathbf{u} + (\nabla \times \mathbf{B}) \times \mathbf{B} - \nabla p + \text{Pm} \Delta \mathbf{u}, \quad (1)$$

$$\frac{\partial \mathbf{B}}{\partial t} = \nabla \times (\mathbf{u} \times \mathbf{B}) + \Delta \mathbf{B}, \quad (2)$$

where \mathbf{u} and \mathbf{B} are the velocity and magnetic fields and p is the pressure. Additionally, the relations $\nabla \cdot \mathbf{u} = 0$ and $\nabla \cdot \mathbf{b} = 0$ hold. The magnetic permeability and the density are set to unity in this system of units. Since all quantities are normalized with the magnetic diffusivity η , the magnetic Prandtl number $\text{Pm} = \nu/\eta$ appears in the momentum equation, where ν is the kinematic viscosity. Velocities are normalized by η/R , times by R^2/η .

For Steps I and III, the differential rotation and the poloidal magnetic field are initial conditions. They evolve freely without any further imposed properties. The profile of the initial angular velocity follows

$$\Omega(s) = \frac{\Omega_0}{\sqrt{1+s^q}}, \quad (3)$$

where Ω_0 is the non-dimensional angular velocity on the axis and q is a parameter controlling the steepness of the rotation profile. With our normalization, the initial magnetic Reynolds number is actually $\text{Rm} \equiv \Omega_0$, since

$$\text{Rm} = \frac{R^2 \Omega_*}{\eta}, \quad (4)$$

where Ω_* is the angular velocity of the star in physical units. The magnetic Reynolds number was $\text{Rm} = 20\,000$ in all computations except one; the magnetic Prandtl number was always $\text{Pm} = 1$.

The pre-main-sequence evolution of the rotation period of intermediate-mass stars contains most likely both a spin-up (contraction and accretion) phase and a spin-down phase with magnetized winds (Stępień 2000). We are concerned with the evolution near the end of the pre-main-sequence phase and the early main-sequence life when most of the star is already radiative (convectively stable). The probable angular-momentum change is a spin-down then, acting on the surface of the star, and this is the reason why we assumed an angular velocity *decreasing* with axis distance. The initial profile uses $q(t = 0) = 4$, but q will later be

used to measure the actual steepness of the rotation curve in the simulation. The specific angular momentum $s^2\Omega(s)$ is increasing with axis distance everywhere in the computational domain. The system is thus not prone to the hydrodynamic Rayleigh instability which we do not want to investigate here. The hydrodynamic stability has been tested numerically with non-axisymmetric perturbations which were symmetric and anti-symmetric with respect to the equator. All situations delivered a decay of the perturbations.

Magnetic fields are measured in terms of Lundquist numbers, which is the same as the non-dimensional Alfvén velocity in our system of units,

$$B = \frac{RB_{\text{phys}}}{\sqrt{\mu\rho\eta}}. \quad (5)$$

The magnetic diffusivity η in time-dependent simulations typically represents a value between the microscopic diffusivity of the plasma and the turbulent diffusivity resulting from, e.g., averaged convective motions. Of the quantities entering (5), η is the one which is known least. It is therefore best to eliminate η by Rm and thus retrieve the physical magnetic fields by comparing its Alfvén speed with the rotational velocity,

$$B_{\text{phys}} = \sqrt{\mu\rho}\Omega_{\text{phys}}R\frac{B}{\text{Rm}} \quad (6)$$

Considering a $2M_{\odot}$ star with a radius of $R_* = 1.5R_{\odot}$, a rotation period of 10 days ($\Omega_{\text{phys}} = 7.3 \cdot 10^{-6}$) and a density of 0.015 g/cm^3 at $0.75R_*$, a magnetic field of $B = 100$ converts to 1660 G in physical units with the magnetic Reynolds number of 20 000 used in most of our simulations.

The boundary conditions for all runs presented here employ stress-free conditions for the flow and vacuum conditions for the magnetic field at both the inner and outer radii, r_i and r_o . Although the inner sphere is supposed to be highly conducting, a vacuum condition helps in obtaining smoother solutions compared to a superconducting condition. The latter prohibits a penetration of the magnetic field through the inner boundary. This typically leads to strong currents near the inner boundary which are not there if the conductivity would change continuously into the inner sphere. If, for efficiency reasons, the whole star cannot be computed, the vacuum condition is a suitable choice despite the non-vanishing conductivity. We will come back to a test run with a perfect-conductor boundary at r_i in Section 5.

Note that the assumption of an initially independent angular velocity of the vertical axis $z = r \cos \theta$ (Taylor-Proudman state) is not compatible with a stress-free condition on a spherical surface. This causes small meridional flows and results in a small deviation from the Taylor-Proudman state. However, this is a much better choice than an initial rotation profile depending on r which causes a severe redistribution of angular momentum towards a configuration which is very near a Taylor-Proudman state during the first rotations of the system. As we did not want to obtain a mixed evolution of this hydrodynamic phenomenon with the magnetic phenomena, we chose $\Omega(s)$ instead of more complicated profiles $\Omega(r, \theta)$.

The spin-down by winds during the late pre-main-sequence phase of intermediate-mass stars is probably not causing a precise $\Omega(s)$ profile, but for the sake of physical clarity, we choose a Taylor-Proudman state as an initial condition for the runs. Note that the removal of angular momentum by a magnetized wind is not implemented in our setup, so the simulations can be understood as mimicking a period around the time when the star enters the main sequence.

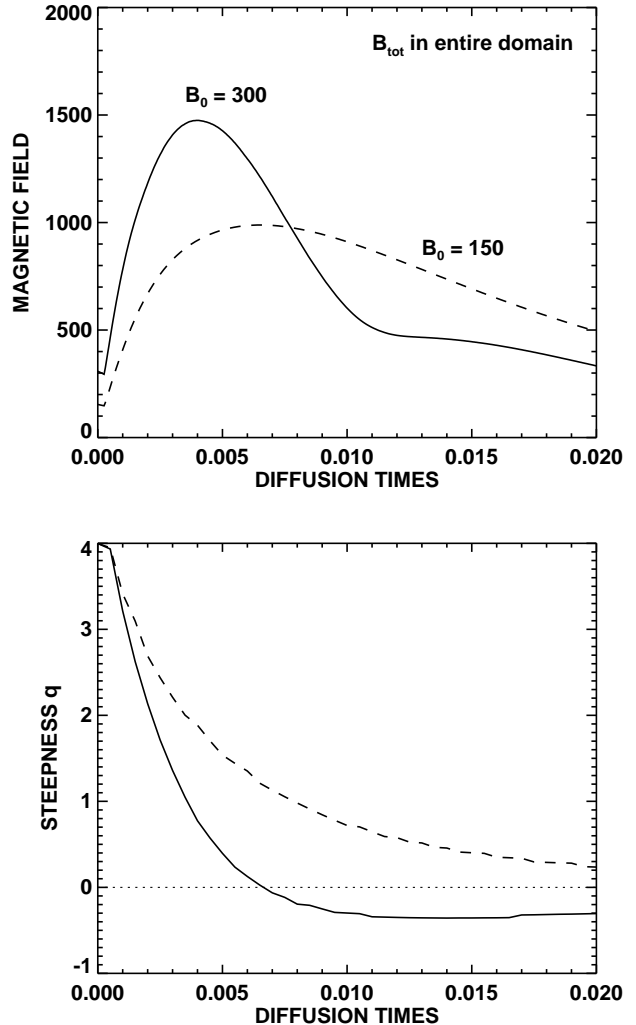


Figure 1. Amplification of the toroidal magnetic field under the influence of differential rotation, starting from a poloidal field. The solid line refers to an initial maximum magnetic field strength of 300, the dotted line is the evolution of an initial field strength of 150.

3 AXISYMMETRIC EVOLUTION (STEP I)

First we study the amplification of magnetic fields by shear as well as the back-reaction of the fields on the differential rotation. The two-dimensional, non-linear simulations thus start with an initial differential rotation and a purely poloidal magnetic field in a radiative stellar zone. These initial conditions evolve freely without any imposed flows or fields, neither in the bulk of the computational domain nor at the boundaries.

The early phase of the simulation shows a generation and steep amplification of toroidal magnetic field through differential rotation. The generated $B_r B_\phi$ and, to a smaller extent, also the $B_\theta B_\phi$ impose a Lorentz force to the rotational velocity and redistributes angular momentum. This is why at the same time of field amplification, the differential rotation starts to decrease, and the toroidal-field growth is thus limited. The whole process reaches a maximum of magnetic field energy after a few rotational periods.

Fig. 1 shows the maximum magnetic field in the spherical shell as a function of time. The magnetic Reynolds number was $\text{Rm} = 20\,000$ and the magnetic Prandtl number was $\text{Pm} = 1$.

Two runs with initial, purely poloidal magnetic fields with maximum strengths of $B_0 = 300$ and $B_0 = 150$ are shown. The lower panel of the Figure shows the decay of the differential rotation. We assume that the differential rotation roughly follows a profile (3) throughout the simulation, with varying parameters Ω_0 and q . The values of $\Omega(s)$ in the equatorial plane of each snapshot of the simulation are used to fit a best profile (3) delivering two time series for $\Omega_0(t)$ and $q(t)$. It is the temporal evolution of q which is shown in the lower panel of Fig. 1. Interestingly, the run with a stronger initial poloidal magnetic field shows a reversal of the differential rotation profile after 0.006 diffusion times. Only after a very long period, not plotted here, the shear converges to zero in the entire computational domain.

Maximum internal field strengths are about 24 kG in the run with $B_0 = 300$ and about 16 kG in the run with $B_0 = 100$, using the conversion (6). Much higher magnetic Reynolds numbers encountered in real stars lead to stronger toroidal fields. A run with $Rm = 40\,000$ later described in Section 5 reached about 46 kG.

The amplification time results from the comparison of the Lorentz force acting on the differential rotation with the generation of toroidal magnetic field by the shear. The linearized action of the Lorentz force may be approximated by $\Delta\Omega \sim \Delta t B_r B_\phi / \mu \rho R$ and the linear winding up of toroidal field in the induction equation can be estimated by $B_\phi \sim \Delta t \Delta\Omega B_r / R$. Plugging the B_ϕ into the first relation, delivers $\Delta t = R \sqrt{\mu \rho} / B_r$. The amplification time is independent of the rotation rate, the amplitude of the differential rotation, and the diffusivity. In our dimensionless system, the amplification time is thus $\Delta t = 0.0033$ for the initial field of $B_0 = 300$. This is very close to the peak time of the solid line in Fig. 1. The dashed curve from half the initial field strength peaks at roughly twice that period – a bit earlier since diffusion and hydrodynamic redistribution of angular momentum are also at play in this numerical setup. There is a slight tendency of smaller magnetic Reynolds numbers producing shorter times to reach the peak magnetic field. This is solely due to the non-vanishing viscosity, being present in our system of finite Rm , which adds to the reduction of the differential rotation and limits the growth eventually.

A real system with stellar microscopic diffusivities of say $\eta = 1000 \text{ cm}^2/\text{s}$ will show a nearly stationary phase after the amplification, since the Ohmic decay times are of order gigayears. A time-dependent numerical simulation cannot model the very low diffusivity at the true rotation rate, and the solution is subject to a much larger Ohmic dissipation after the maximum toroidal field is reached. The following process is thus characterized by a decay of both magnetic fields and differential rotation. Since the simulations preserve angular momentum parallel to the rotation axis, the asymptotic state is field-free and with uniform rotation. We are not interested in this asymptotic behaviour. Intermediate-mass stars are not living long enough to show this final state during their evolution on the main sequence.

4 NON-AXISYMMETRIC, LINEAR STABILITY (STEP II)

Differential rotation and rotation in general stabilize any current-driven instabilities (Taylor instability) as was shown by Rüdiger & Kitchatinov (2010). Differential rotation together with diffusion has a destructive effect on any non-axisymmetric structures. At some point during the amplification of magnetic fields by shear, the axisymmetric solution of Section 3 may become unstable against non-axisymmetric perturbations, as soon as the stabilizing effect of the differential rotation ceases.

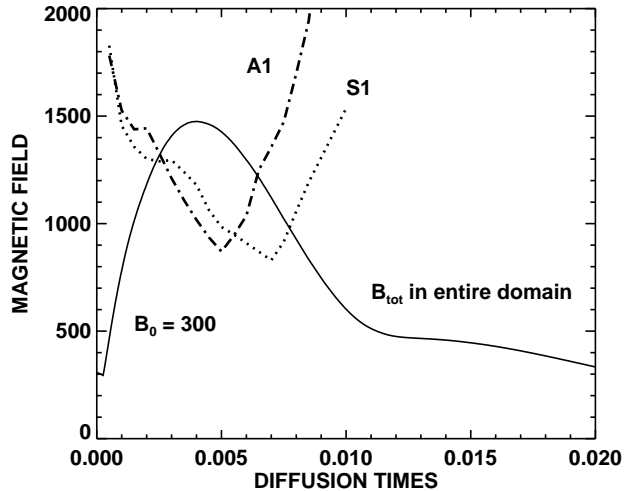


Figure 2. Stability limits for the magnetic fields and velocity fields of each snapshot of the axisymmetric evolution of the $B_0 = 300$ case. The solid line is copied from Fig. 1. The stability limit is plotted for a perturbation of $m = 1$, the dotted line refers to a perturbation whose velocity field is symmetric with respect to the equator, the dash-dotted line shows the axisymmetric perturbation.

Each snapshot of the run with $B_0 = 300$ from Section 3 was thus tested individually on whether or not a non-axisymmetric perturbation can grow on the particular axisymmetric configuration. However, from the snapshots, only the azimuthal velocity and the toroidal magnetic field, u_ϕ and B_ϕ , are used for the stability analysis. The full problem was found to be numerically demanding and is postponed to a future study. The final conclusions are not affected by this simplification.

We consider the linearized equations for a given azimuthal wave number m . The snapshots delivered background states in \mathbf{u} and \mathbf{B} which affect the perturbation $(\mathbf{u}', \mathbf{B}')$ and lead to exponential growth or decay of the perturbation.

The stability analysis is based on the linear, normalized MHD equations

$$\begin{aligned} \frac{\partial \mathbf{u}'}{\partial t} &= \left[\mathbf{u}' \times \nabla \times \mathbf{u} + \mathbf{u} \times \nabla \times \mathbf{u}' - \nabla(\mathbf{u}' \cdot \mathbf{u}) \right] \\ &\quad + S \left[(\nabla \times \mathbf{B}') \times \mathbf{B} + (\nabla \times \mathbf{B}) \times \mathbf{B}' \right] \\ &\quad - \nabla p + \text{Pm} \Delta \mathbf{u}', \end{aligned} \quad (7)$$

$$\frac{\partial \mathbf{B}'}{\partial t} = \nabla \times (\mathbf{u} \times \mathbf{B}' + S \mathbf{u}' \times \mathbf{B}) - \Delta \mathbf{B}', \quad (8)$$

again with $\nabla \cdot \mathbf{u}' = 0$ and $\nabla \cdot \mathbf{B}' = 0$. The constant density ρ and the magnetic permeability μ are also unity in this normalization. S is a factor which scales the total background magnetic field taken from the axisymmetric run. The critical S for instability is determined. The background is unstable, if $S > 1$. Note that we do not evolve the system actually in time: the axisymmetric background velocity and magnetic fields are constant. The time-dependence appears here solely for the test on growing or decaying perturbations.

The dotted and dot-dashed lines in Fig. 2 are the results of the stability analysis. The evolution derived from the axisymmetric simulation starting with an initial maximum field strength of 300 is taken from Fig. 1 and is plotted as a solid line. By S1 we refer to a velocity perturbation \mathbf{u}' which is symmetric with respect to the equator and has $m = 1$, A1 is the corresponding antisym-

Table 1. Four non-linear simulations with their parameters as discussed in Sections 5 and 6. The truncations for the Chebyshev, Legendre, and Fourier modes are given as K , L , and M , respectively. The column t_{pert} gives the time when the non-axisymmetric perturbation was injected into the system, expressed in diffusion times.

Run	Rm	Pm	$K \times L \times M$	t_{pert}
NL000	20000	1	$35 \times 80 \times 80$	0
NL003	20000	1	$40 \times 60 \times 60$	0.003
NL003h	40000	1	$40 \times 60 \times 60$	0.003
NL005	20000	1	$40 \times 60 \times 60$	0.005

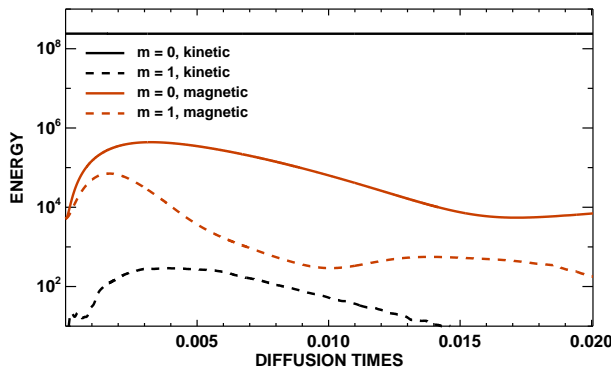


Figure 3. Evolution of a non-axisymmetric perturbation added to the axisymmetric run of Fig. 1 at $t = 0$.

metric perturbation. If at any given time both stability lines are above the solid line, the corresponding snapshot is stable against $m = 1$ perturbations. The first snapshots with relatively weak toroidal fields are all stable. The stability lines cross the solid one at about $t = 0.0023$. There is a minimum marginal stability at $t = 0.0055$ for the S1 mode, and at $t = 0.0070$ for the A1 mode.

After these times, the stability limits increase again. The stabilization may be due to the change of sign in the shear. The differential rotation is then non-vanishing again and may impose a stabilizing effect on perturbations despite its relatively small, positive amplitude.

Higher m require similar magnetic fields for instability as was shown in test runs with $m = 2$.

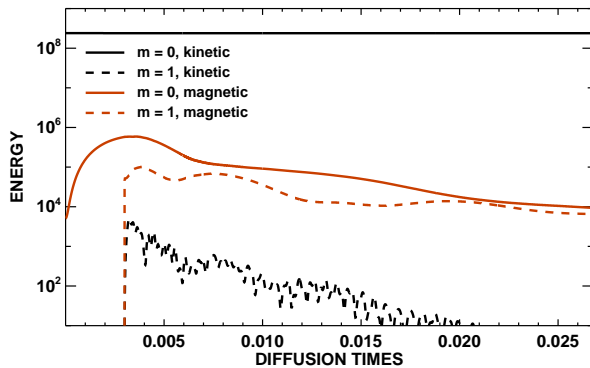


Figure 4. Evolution of a non-axisymmetric perturbation added to the axisymmetric run of Fig. 1 at $t = 0.003$.

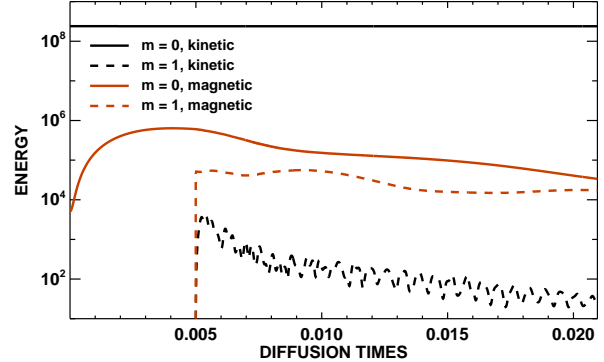


Figure 5. Evolution of a non-axisymmetric perturbation added to the axisymmetric run of Fig. 1 at $t = 0.005$.

5 NON-LINEAR EVOLUTION IN 3D (STEP III)

The initial conditions are the same as for Section 3, but the system is now extended to include also a Fourier decomposition of \mathbf{u} and \mathbf{B} in azimuthal direction. The main difference is a non-axisymmetric perturbation hitting the system at a given time t_0 . The perturbation is applied to \mathbf{B} , has an azimuthal wave number of $m = 1$ and is symmetric with respect to the equator, i.e. $B'_r(\theta) = B'_r(\pi - \theta)$, $B'_\theta(\theta) = -B'_\theta(\pi - \theta)$, and $B'_\phi(\theta) = B'_\phi(\pi - \theta)$. The resulting flow is thus antisymmetric and can be compared with the A1-mode in the linear stability diagram in Fig. 2. A small overview of the models is given in Table 1.

Figs. 3–5 show the evolution of the energies of the lowest azimuthal modes, $m = 0$ and $m = 1$, for three different instances of perturbations, $t = 0$, $t = 0.003$, and $t = 0.005$. The main feature of the run with the perturbation at the beginning is the quicker decay of the energy in the non-axisymmetric magnetic field as compared with the other two simulations. Their perturbations at $t = 0.003$, and $t = 0.005$ are within the unstable window (cf. Fig. 2) and show a much more persistent presence in the system. The energy of the magnetic $m = 1$ mode may even become nearly as large as the magnetic $m = 0$ energy. It is interesting to note that the energy in the $m = 1$ mode of the velocity field decays more rapidly than the magnetic energy in both unstable cases.

Typical horizontal slices of the velocity and magnetic fields are shown in Fig. 6. They are plotted for $r = 0.75$ which is half-way between the inner and outer radial boundaries. Azimuthal mode numbers $m > 1$ are obviously at play, but we cannot talk about a turbulent state here. The $m = 2$ contains roughly half the magnetic energy of the $m = 1$ mode throughout the simulation. An example spectrum for the kinetic and magnetic energies of all individual m -modes is shown in Fig. 7. The energy in the $m = 4$ mode is already two orders of magnitude smaller than the energy in $m = 1$. The total contrast between $m = 1$ and $m = 60$ is 10^{10} in the kinetic energy and one order of magnitude higher in the magnetic energy. Strongest magnetic fields appear to be concentrated in low latitudes. Since the axisymmetric parts of \mathbf{u} and \mathbf{B} were subtracted before plotting Fig. 6, the surface maps also reflect the energy ratio of magnetic $m = 1$ energy to kinetic $m = 1$ energy. While the ratio of $|B_r|$ to $|u_r|$ is 5.3, the energy ratio would be almost 30, being compatible with the $m = 1$ energy ratio in Fig. 4 between $t = 0.003$ and $t = 0.005$. The magnetic fluctuations are dominating over the velocity fluctuations in these simulations.

The impact of the non-axisymmetric instability on the rota-

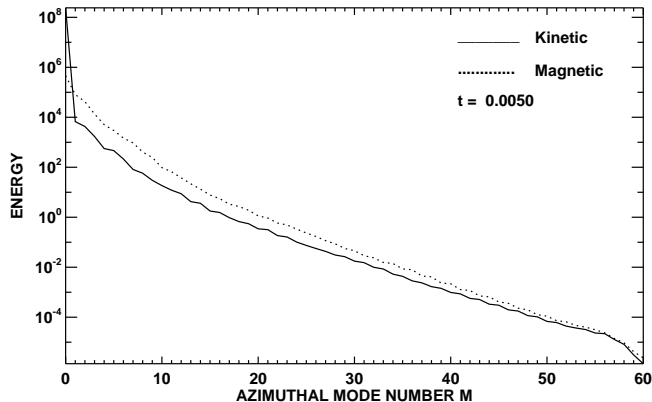


Figure 7. Distribution of kinetic energy (solid line) and magnetic energy (dotted line) over the azimuthal wave number m for the run NL003 at $t = 0.005$, i.e. 0.002 diffusion times after the perturbation was injected.

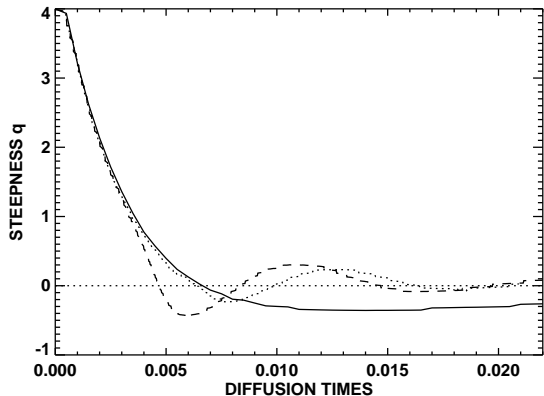


Figure 8. Variation of the steepness of the rotation profile with time: the solid line is the result from the axisymmetric run and is the same curve as in Fig. 1; the dashed line is the result from the non-linear run with a non-axisymmetric perturbation at $t = 0.003 = 9.5P_{\text{rot}}$, and the dotted line is for a perturbation at $t = 0.005 = 15.9P_{\text{rot}}$.

tion profile is shown in Fig. 8. An enhanced angular momentum transport to reduce the differential rotation is only notable for the simulation with a perturbation at $t = 0.003$. The most obvious difference between the unperturbed run and the unstable runs is the time it takes to reach fully uniform rotation. Both perturbed simulations reach a state of uniform rotation after 0.017 diffusion times, while it takes the axisymmetric run about 0.05 diffusion times to be similarly uniform in rotation (outside the plotting window).

6 DYNAMO EFFECT

The following section is not directly related to the pre-main-sequence evolution of Ap stars. We are interested in a possible dynamo effect arising from the instability, since this will open very interesting possibilities of magnetic-field generation in various contexts. We are not proposing the dynamo effect to be overly important for Ap stars.

The non-linear interaction of the unstable $m = 1$ mode may generate an axisymmetric amplification effect of poloidal fields out of toroidal fields. In that case, the Tayler instability would provide a

closed dynamo loop besides the generation of toroidal fields by differential rotation. Sustained dynamo action is conceivable as long as there is a mechanism that sustains differential rotation, whence toroidal fields prone to instability. Rotating convection zones are such providers of differential rotation, for example.

It is assumed here that the dynamo action can be described by a non-vanishing turbulent electromotive force (EMF) delivering a large-scale axisymmetric magnetic field from the non-axisymmetric instability state (which is not necessarily a turbulent state). Everything axisymmetric is considered large-scale, all non-axisymmetric contributions are considered small-scale in this context. We are also assuming that the mean-field coefficients only relate the large-scale magnetic field $\overline{\mathbf{B}}$ and its first derivatives with the EMF, and use the decomposition

$$\begin{aligned} \text{EMF} = & \alpha \overline{\mathbf{B}} + \gamma \times \overline{\mathbf{B}} - \beta (\nabla \times \overline{\mathbf{B}}) \\ & - \delta \times (\nabla \times \overline{\mathbf{B}}) - \kappa (\nabla \overline{\mathbf{B}})^{(\text{sym})} \end{aligned} \quad (9)$$

into symmetric α - and β -tensors, the vectors γ and δ , and the third-rank tensor κ acting on the symmetric part of the tensor gradient of $\overline{\mathbf{B}}$.

When restricting to the diagonal elements of α , one notes that only $\alpha_{\phi\phi}$ can cause an axisymmetric growth of the large-scale poloidal magnetic field from an axisymmetric large-scale toroidal field. Remember that the non-axisymmetric Tayler instability is now supposed to be hidden in the mean-field coefficients, and is not explicitly visible in this description. As long as we are looking for the driving of an axisymmetric dynamo, the existence of the Tayler instability and its properties are supposed to be entirely comprised by the mean-field coefficients.

6.1 Existence of an $\alpha_{\phi\phi}$

Our first attempt to look for dynamo action thus consists of searching for a correlation between the ϕ -component of the turbulent electromotive force, $\text{tEMF} = \langle \mathbf{u}' \times \mathbf{B}' \rangle_{\phi}$, and the ϕ -component of the large-scale magnetic field, $\langle B_{\phi} \rangle$. The brackets refer to suitable averages in space and, ideally, also in time. We simplify the analysis further by using the azimuthal direction for the spatial average and discard time averages. This type of averaging will be denoted by overbars, hence $\text{tEMF}_{\phi} = \overline{(\mathbf{u}' \times \mathbf{B}')_{\phi}}$ and $\overline{B_{\phi}}$. The angular brackets will be used for averages over entire hemispheres of the computational domain in the following.

Instead of averaging over time, we rather look at the temporal evolution of the correlation between tEMF_{ϕ} and B_{ϕ} . The fluctuating quantities are thus derived by $\mathbf{u}' = \mathbf{u} - \overline{\mathbf{u}}$ and $\mathbf{B}' = \mathbf{B} - \overline{\mathbf{B}}$, where overbars are always ϕ -averages. The values of the average turbulent EMF and $\overline{B_{\phi}}$ deliver scatter plots from all the radial and latitudinal grid points of an entire hemisphere. The slope of the regression line as to represent $\alpha_{\phi\phi}$ and the correlation coefficient were derived from these sets of pairs $\{\text{tEMF}_{\phi}(r, \theta), \overline{B_{\phi}}(r, \theta)\}$ from each snapshot in time and each individual simulation.

We also computed the kinetic helicity in the two hemispheres (N and S) from the velocity fluctuations by

$$\mathcal{H}_N = \langle \mathbf{u}' \cdot \text{curl} \mathbf{u}' \rangle_N, \quad \mathcal{H}_S = \langle \mathbf{u}' \cdot \text{curl} \mathbf{u}' \rangle_S, \quad (10)$$

where averages are taken over entire hemispheres. It will be interesting to see to which extent the kinetic helicity is related to what we measure as an α -effect. Turbulence driven by convection leads to an

$$\alpha = -\frac{1}{3} \tau_{\text{cor}} \langle \mathbf{u}' \cdot \text{curl} \mathbf{u}' \rangle, \quad (11)$$

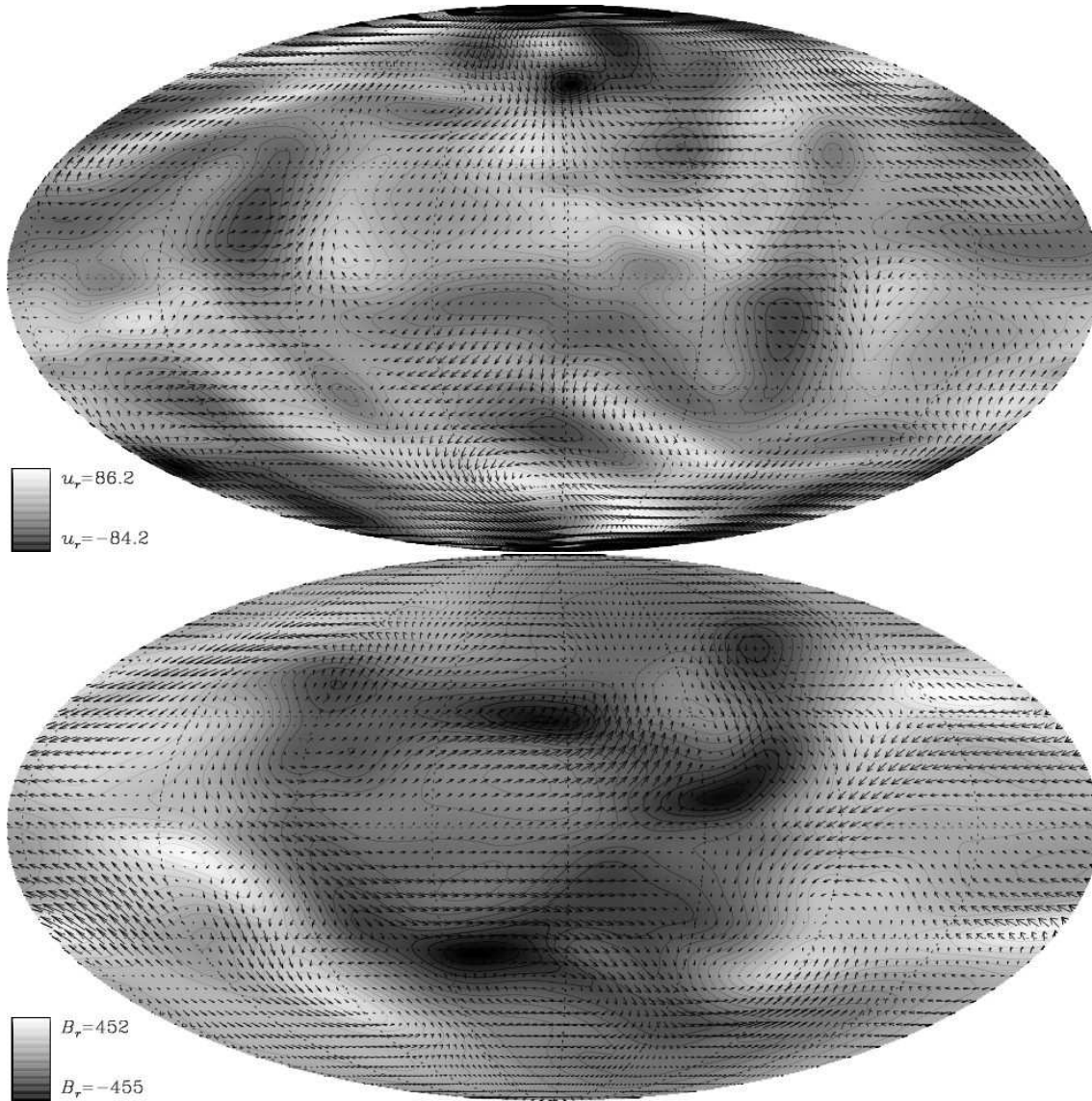


Figure 6. non-axisymmetric velocity field (top) and magnetic field (bottom) at $r = 0.75$ and $t = 0.005$ from run NL003. The axisymmetric parts (fast rotation and strong toroidal magnetic field) were subtracted from the snapshot before plotting. The contours represent the radial components, while the arrows are the projected field directions on the (θ, ϕ) -surface. Note that the actual resolution for the computation of the non-linear terms in both horizontal directions, θ and ϕ , is twice as high as plotted here.

where τ_{cor} is the correlation time. This has also been shown in various simulations (e.g. Giesecke, Ziegler & Rüdiger 2005; Käpylä, Korpi & Brandenburg 2009). Finally, the root mean square (rms) values of the velocity fluctuations are computed for the entire computational domain for the same snapshots in time.

We will again refer to the three simulations with perturbations at $t = 0$, $t = 0.003$, and $t = 0.005$. We recall that in the first one, the perturbation was added to a linearly stable state while in the other simulations, the perturbations were added to linearly unstable cases. In the last case, the toroidal field was already past its maximum value of $\overline{B}_\phi = 1434$, but had still a supercritical strength of $\overline{B}_\phi = 1361$ (we recall that the maximum initial poloidal field strength was $B_0 = 300$ for comparison).

Fig. 9 shows the estimate of $\alpha_{\phi\phi}$ for the run NL000 with a non-axisymmetric perturbation at $t = 0$ when no toroidal fields were present initially. The evolution of this estimate of $\alpha_{\phi\phi}$ is com-

pared with measurements of the kinetic helicity and the rms-values of the velocity components. The initial $\alpha_{\phi\phi}$ is solely due to the initial perturbation interacting with the system after the first time-step. The $\alpha_{\phi\phi}$ dies out very quickly – in about one rotation period – and oscillates around zero with negligible amplitude. The values of $\alpha_{\phi\phi}$ are then about 200 times smaller than the rms velocity. The correlation coefficient of the two quantities $t\text{EMF}_\phi$ and \overline{B}_ϕ in the second panel of Fig. 9 is very close to zero all the time. Open symbols are actually those cases for which the hypothesis of uncorrelated quantities, i.e. no α -effect, holds statistically. The correlation may be still significant for the filled triangles. The limit was set such that there is a remaining probability of 1 per cent for the filled symbols to represent uncorrelated quantities.

The helicity measured compares well with the rms velocity of about 50 and the assumption that the length-scale for the vorticity is roughly $r_o - r_i$, whence $\langle u'^2 \rangle / (r_o - r_i) = 5000$. The length-scale

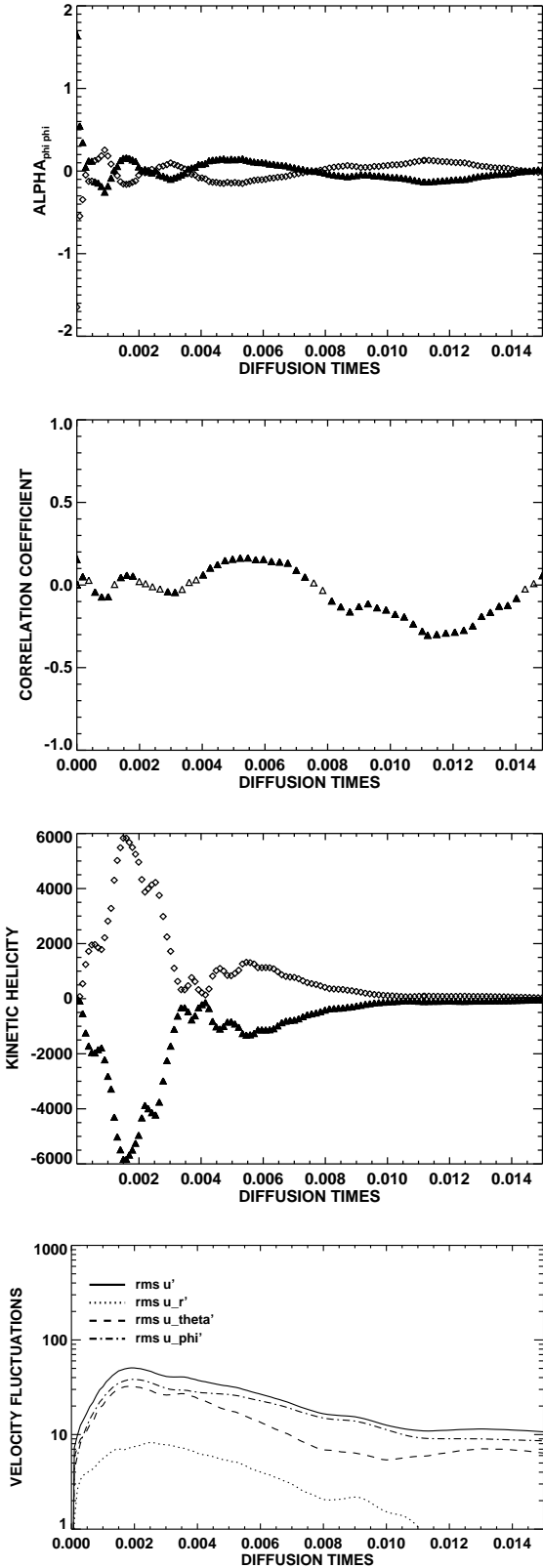


Figure 9. Dynamo-effect (top-panel) expressed as $\alpha_{\phi\phi}$ measured from the simulation with a perturbation at $t = 0$. Only an initial period of the full run of 0.015 diffusion times length is shown here to make the very short presence of non-zero $\alpha_{\phi\phi}$ visible. The second panel shows the correlation coefficient between the turbulent electromotive force and \overline{B}_ϕ , the third panel shows the kinetic helicity and the bottom panel the rms values of the velocity fluctuations.

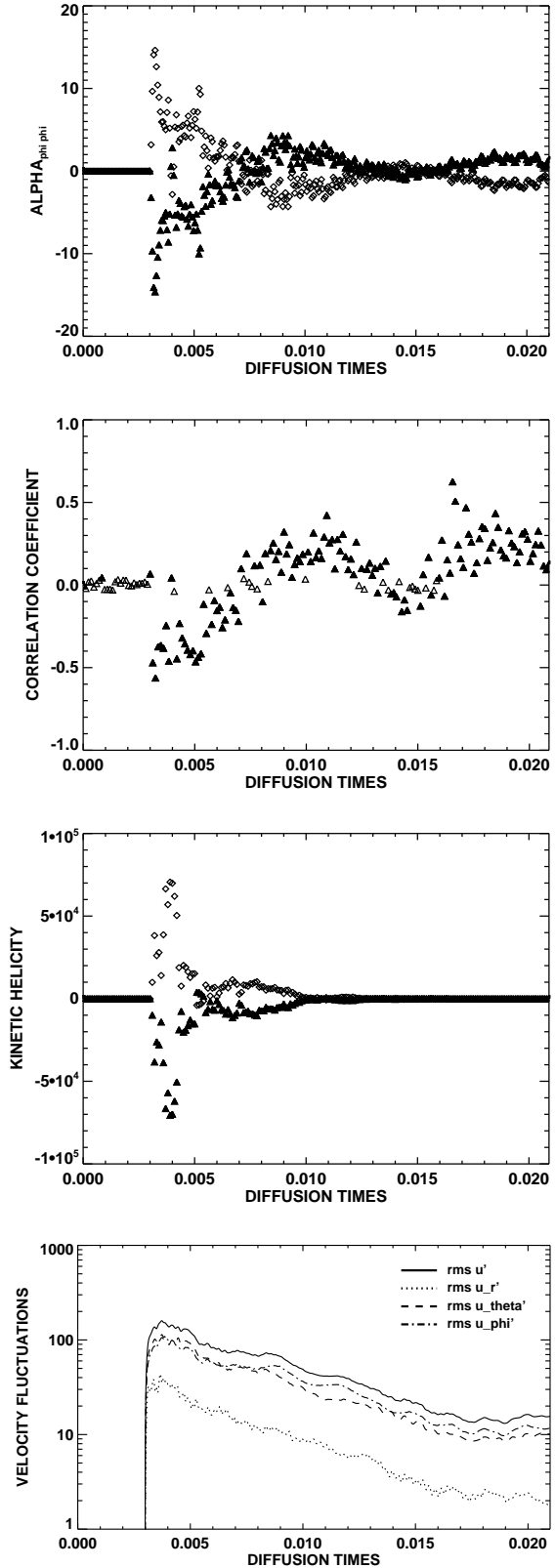


Figure 10. Dynamo-effect (top-panel) expressed as $\alpha_{\phi\phi}$ measured from the simulation with a perturbation at $t = 0.003 = 9.5P_{\text{rot}}$. Again, the second panel is the correlation coefficient, the middle panel shows the kinetic helicity and the bottom panel the rms values of the velocity fluctuations. Note that the period covered by these plots is longer than in Fig. 9 and covers about 67 rotation periods.

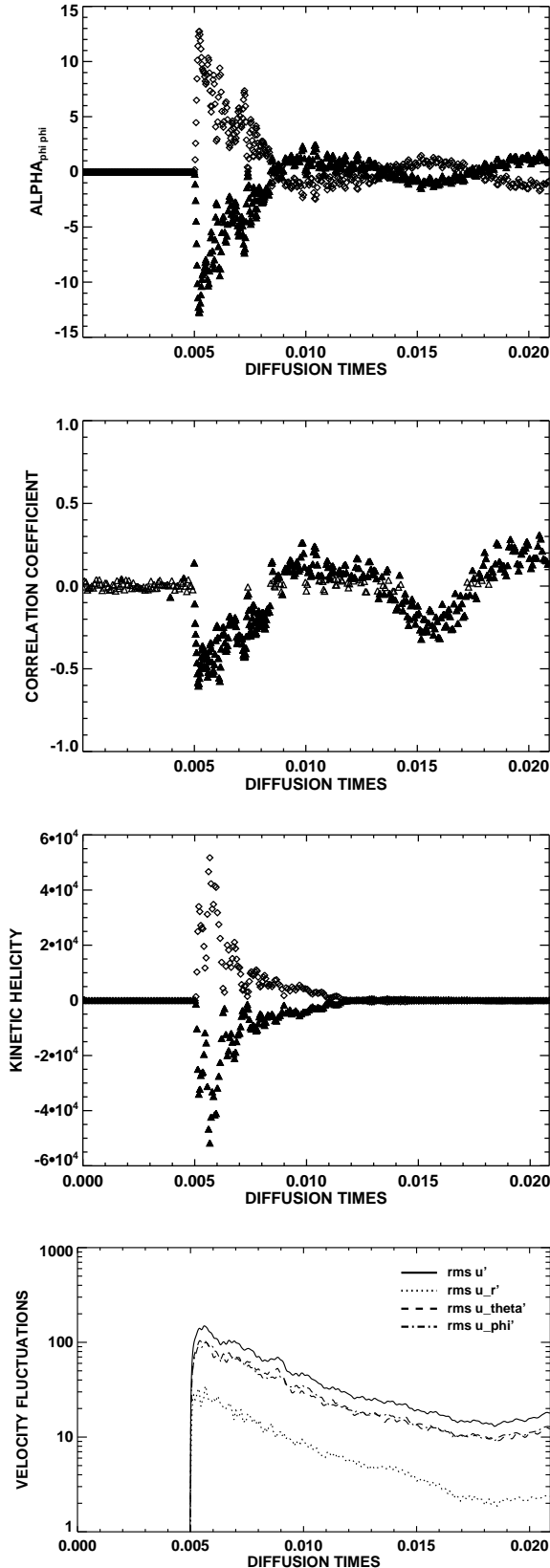


Figure 11. Dynamo-effect (top-panel) expressed as $\alpha_{\phi\phi}$ measured from the simulation with a perturbation at $t = 0.005 = 15.9P_{\text{rot}}$. Again, the middle panel shows the kinetic helicity and the bottom panel the rms values of the velocity fluctuations.

is probably slightly smaller than the thickness of the spherical shell. We also note that the non-axisymmetric motions are dominated by their horizontal components.

The second set of plots in Fig. 10 is from model NL003 with a perturbation at $t = 0.003$ which is a bit more than two rotation periods after the magnetic field has reached its Tayler-unstable strength. The values of $\alpha_{\phi\phi}$ are about 10 times stronger than in model NL000, and they are actually increasing during a short period of about one rotation. The helicity is more than 10 times stronger than in model NL000 and has the same sign as $\alpha_{\phi\phi}$ until $t \sim 0.0075$. The correlation coefficient reaches values of -0.6 . There is apparently a second phase of a small, but significant $\alpha_{\phi\phi}$ which has the opposite sign than the kinetic helicity.

The third set of plots in Fig. 11 shows the simulation NL005 with a perturbation at $t = 0.005$ which is at a time when the axisymmetric toroidal field has a strength of $\overline{B}_\phi = 1361$ and is already decreasing, and the average differential rotation is already near zero. At that time, the linear stability limit is lowest in the whole period considered here. The values of $\alpha_{\phi\phi}$ are a bit lower than those of NL003, but are also first increasing during about one rotation period. Again, the correlation coefficient reaches values around -0.6 in this run. The sign change, which was also present in the $\alpha_{\phi\phi}$ of NL003, takes place at $t = 0.0088$. This is relatively earlier than in NL003, when measured from the perturbation time.

The radial distribution of the α -effect can tell us something about the origin of the dynamo action. If one uses only the values of $\langle \mathbf{u}' \times \mathbf{B}' \rangle_\phi$ and \overline{B}_ϕ for a given r from all the θ -locations in a hemisphere, the resulting correlation will be a local one in radius. We should bear in mind though, that the $\alpha_{\phi\phi}$ become statistically less significant, since we obtain a regression line from 47 grid points only, in the cases of NL003 and NL005. We plot the corresponding distributions of $\alpha_{\phi\phi}$ estimates versus radius for NL003 in Fig. 12 with a perturbation at $t = 0.003$.

Non-zero $\alpha_{\phi\phi}$ are mostly found in the inner half of the spherical shell, at $r < 0.75$. Because of the vacuum condition on the radial boundaries, we do not expect the turbulent EMF to be zero, and the $\alpha_{\phi\phi}$ derived from the regression method thus need not vanish. A run with perfect conductor boundary conditions at r_1 was performed to evaluate the influence of the inner boundary. The $\alpha_{\phi\phi}$ is then indeed zero at the inner boundary. The maximum values of $\alpha_{\phi\phi}$ near $r = 0.6$ are about ± 90 as compared to about ± 110 in NL003. We will show spatial distributions of α -components again below, obtained with another method.

Note that there is no point in looking at the total magnetic energies in these simulations. Since neither the differential rotation nor the initial magnetic field are imposed anywhere in the computational domain, there is no long-lived energy source in the system which could drive a dynamo noticeable in sustained magnetic energies. The concern of this Paper is rather the evolution of stars into objects with apparently stationary magnetic fields, such as magnetic intermediate-mass stars. We are not focusing on sustained dynamo action here.

The spatial distribution of the kinetic helicity and the current helicity is shown in Fig. 13. The concentration of the helicity near the inner boundary resembles the result from the α -measurement which also showed larger values in the inner part of the computational domain. More precisely, we can see that the helicity is actually concentrated near the place where the tangent cylinder touches the inner sphere. The right panel is derived from the run NL003h which has the same parameters as the run NL003, however, with $Rm = 40\,000$. While the picture is more noisy than the one for lower Rm , we also see the the helicity concentration becomes thin-

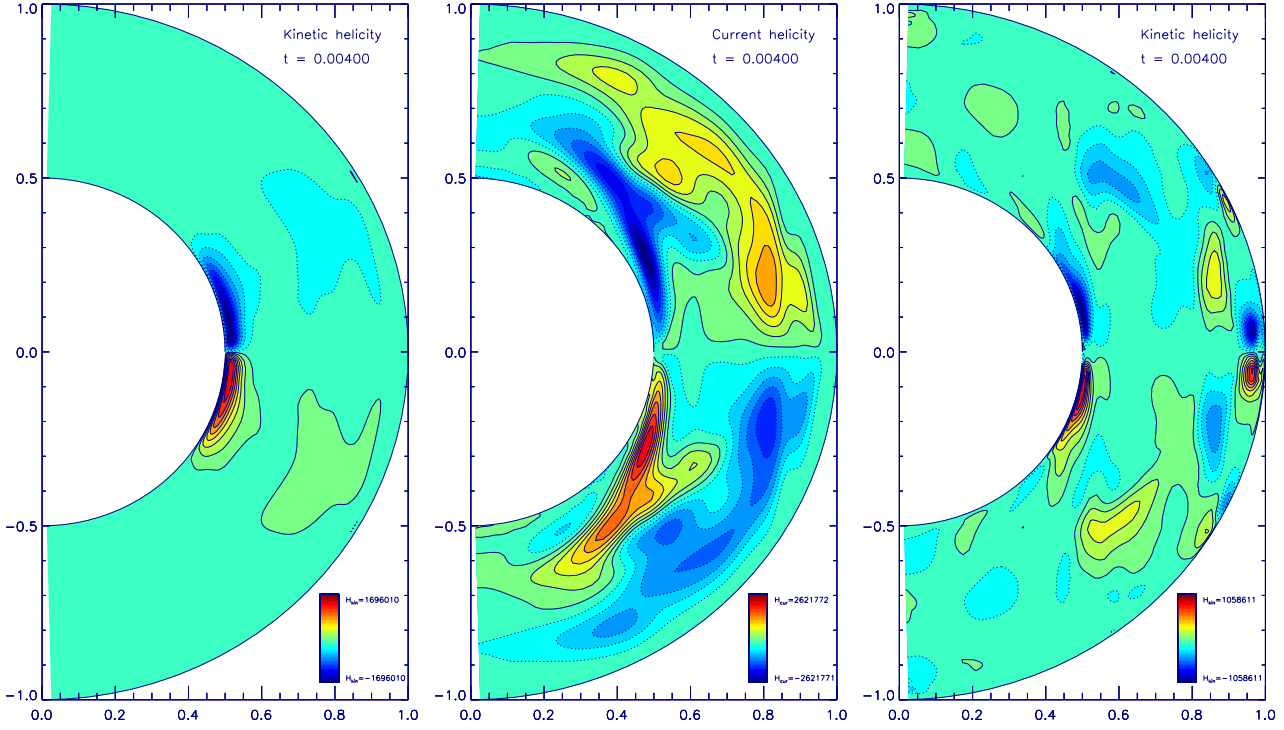


Figure 13. Left: kinetic helicity in the (r, θ) -plane average over the azimuthal direction taken from the run NL003. Middle: current helicity obtained in the same way for NL003. Right: kinetic helicity of the run NL003h with doubled magnetic Reynolds number.

ner with respect to the axis distance. Note that the perturbation of this run actually kicks in at a different stage of super-critically as compared to NL003, because rotation alters the stability limits. In general, however, we have to conclude that a considerable part of the kinetic helicity present in the system is due to the geometrical setup, namely the presence of an inner cylinder. The situation is unchanged in the run with perfect conductor boundary conditions at r_1 .

This is different for the current helicity. A considerable amount of *positive* current helicity is measured in the bulk of the northern hemisphere. We believe that it is mostly this positive current helicity contributing to the small, but positive $\alpha_{\phi\phi}$ -effect in the bulk of the northern hemisphere. The regression method is a bit crude at this point; the below results from the test-field method will show this more clearly.

It is interesting to note that the sign of $\alpha_{\phi\phi}$ and the kinetic helicity is the same in the inner half of the radial extent and especially near the tangent cylinder. This contradiction with (11) is apparently caused by a one-cell helical motion, rather than by an average of turbulent motions. Interestingly, Reshetnyak (2006) also finds negative kinetic helicity along the tangent cylinder, albeit it is a convective, non-magnetic simulation. The feature is more obvious in the run with low Rayleigh number, in which convection is not reaching a turbulent state. We think that the negative helicity near the tangent cylinder of the northern hemisphere is an inner-boundary effect, neither related to convective nor Tayler instability turbulence.

6.2 Mean-field coefficients from the test-field method

The second attempt to look for dynamo action consists of the test-field method as described by Schrunner et al. (2007). In parallel to

the actual non-linear simulation, several equations for a magnetic-field like quantity $\mathbf{b}^{(i)}$ similar to the induction equation are evolved, following the action of the large-scale and small-scale velocity, $\overline{\mathbf{u}}$ and \mathbf{u}' , from the real simulation on given test-fields $\overline{\mathbf{B}}_T^{(i)}$. Because of the similarity of the computational setup use here and of the simulations used by Schrunner et al. (2007), we implemented the test-field method precisely in the same way. Note the different definition of the signs of α and γ in (9) though.

The separation of large-scale and small-scale contributions to \mathbf{u} and is again done by azimuthal averages, leading to a large-scale field depending on r and θ only. Nine different test fields give rise to 27 test-field equations, delivering nine mean electromotive forces $\mathcal{E}^{(i)}$ from \mathbf{u}' and the $\mathbf{b}^{(i)}$. Replacing EMF and $\overline{\mathbf{B}}$ by $\mathcal{E}^{(i)}$ and $\overline{\mathbf{B}}_T^{(i)}$ in (9) leads to a system of equations which can be solved for the mean-field coefficients.

The values of the symmetric α -tensor averaged over time are shown in Fig. 14, taken from the run NL003 and the period from $t = 0.0035$ to $t = 0.0040$. The initial phase of the onset of the instability has thus been omitted. We see that it is α_{rr} which has the strongest peak values, followed by $\alpha_{\theta\theta}$ and $\alpha_{\phi\phi}$. In an axisymmetric mean-field dynamo, α_{rr} and $\alpha_{\theta\theta}$ are generators of the toroidal magnetic field. While $\alpha_{\phi\phi}$ has the same sign as the kinetic helicity near the inner boundary, the other two diagonal elements have the opposite sign. The anisotropy of the α -effect is due to the relatively strong rotation of the system. The numbers can be directly compared to the velocity measurements shown in Fig. 11.

The contributions from the derivatives of $\overline{\mathbf{B}}$ are rather small. The coefficients β_{rr} , $\beta_{\theta\theta}$, and $\beta_{\phi\phi}$ are all positive and do not exceed the order of unity. Interestingly, the contributions from several pairs of coefficients nearly cancel in the construction of the turbulent EMF. In particular, these are $\beta_{r\phi}$ cancelling with $-\delta_\theta$, and $\beta_{\theta\phi}$ with δ_r .

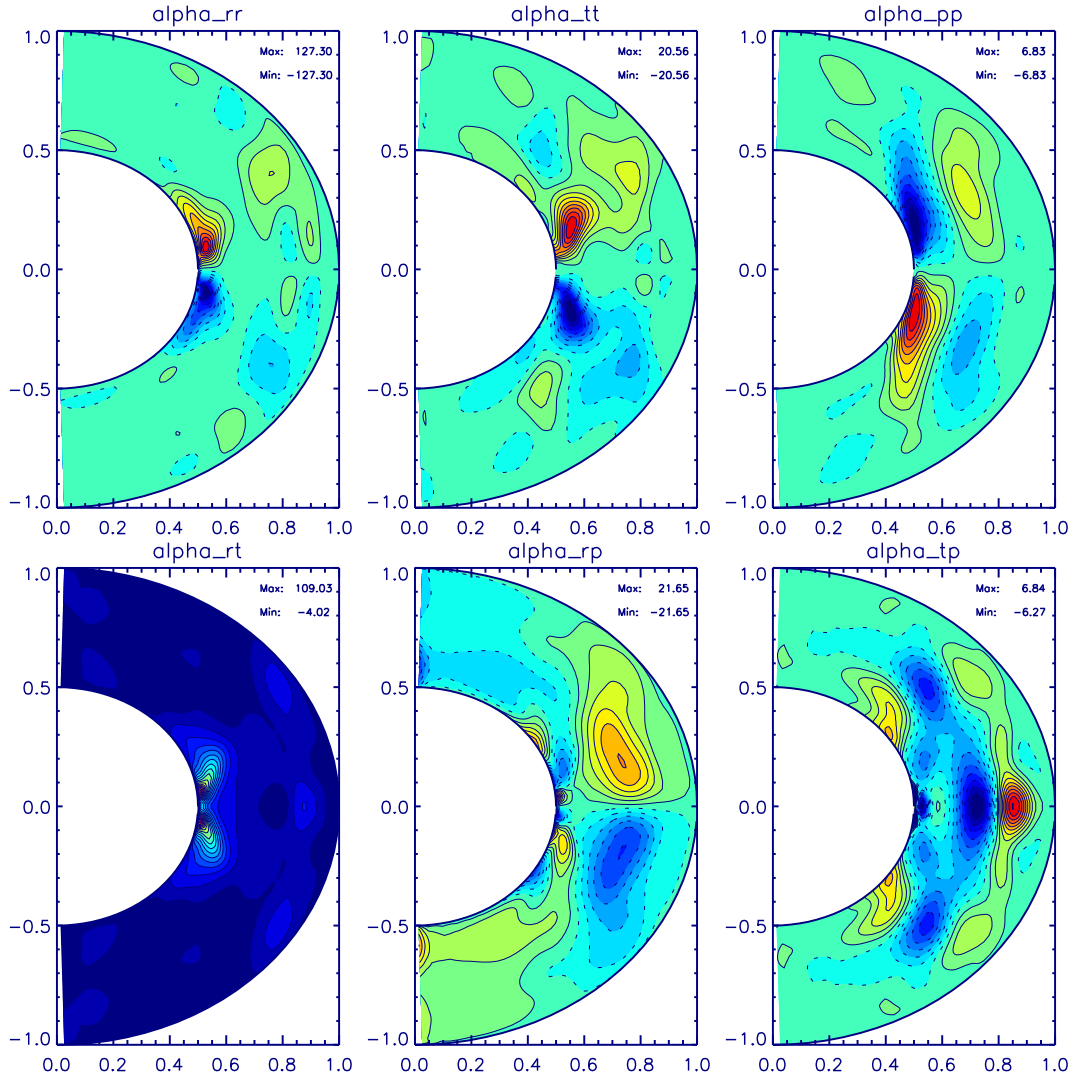


Figure 14. Coefficients of the symmetric α -tensor obtained by the test-field method. Units are in the dimensionless units of velocity of the simulation. The cross-sections shown here are averaged within $t = 0.0035$ and $t = 0.0040$ diffusion times.

6.3 Comparison

Both methods have their disadvantages. On the one hand, the regression method for the determination of $\alpha_{\phi\phi}$ ignores the possible influence of other mean-field coefficients on the ϕ -component of the turbulent EMF. The test-field method, on the other hand, relies on turbulence which is not magnetically driven. Only the velocity field from the actual simulation enters the determination of the mean-field coefficients. Our simulations are concerned with magnetically generated fluctuations \mathbf{u}' and \mathbf{B}' , however. It is therefore very likely that the mean-field coefficients determined by the test-field method are systematically underestimated. A comparison of the rms magnetic fields, $B_{\text{rms}} = \sqrt{\langle B'^2 \rangle}$, with rms velocities, $u_{\text{rms}} = \sqrt{\langle u'^2 \rangle}$, over time reveals a factor of about three between the two for the run NL003.

It is elucidating to compare the turbulent EMF measured from the simulation directly with the turbulent EMF constructed from the mean-field coefficients together with the measured large-scale $\overline{\mathbf{B}}$. The directly measured EMF is about four times larger than the reconstructed EMF. This ratio is very similar to the above mentioned ratio of B_{rms} to u_{rms} . The current helicity shown in Fig. 13 in the

shell from $r = 0.75$ to $r = 0.95$ is even ten times larger than the kinetic helicity in the same region.

7 SUMMARY AND DISCUSSION

We studied the amplification and stability of magnetic fields in the pre-main-sequence evolution of intermediate-mass stars. Especially the phase when the stars possess an extensive radiative envelope already is considered. The amplification of a poloidal magnetic field by differential rotation is studied in a non-convective, spherical shell. The feedback by the Lorentz force diminishes the differential rotation brings the field growth to a halt. The amplification time and amplitude only depend on the initial, poloidal magnetic field. The amplification time is given by

$$\Delta t \approx R\sqrt{\mu\rho}/B_r \quad (12)$$

and results to about 7500 yr for a star with $R = 3R_{\odot}$, $\rho = 0.1 \text{ g cm}^{-3}$, and an initial magnetic field strength of $B_r = 1 \text{ G}$. These time-scales are very short, but one needs to bear in mind that the stellar winds in this phase of the evolution will still remove

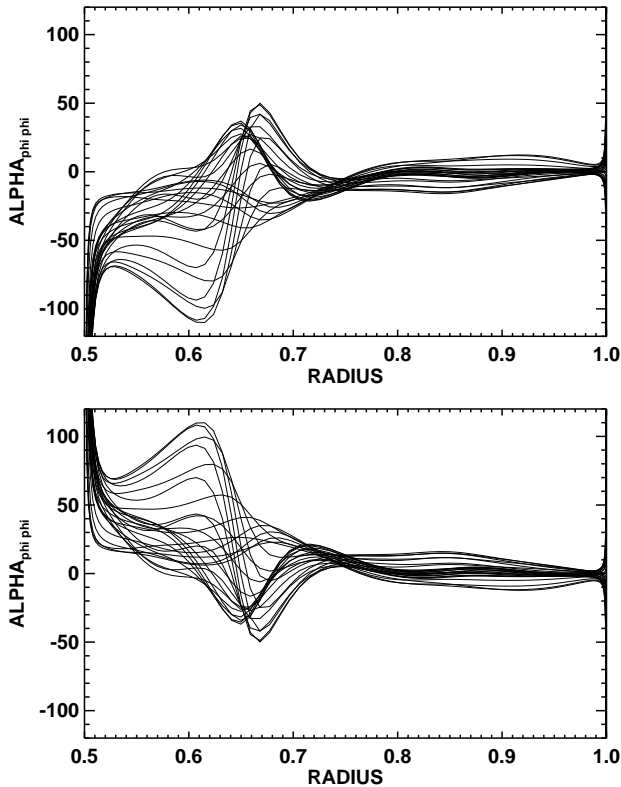


Figure 12. Dynamo-effect in terms of α_{ϕ} versus radius measured from the simulation with a perturbation at $t = 0.003 = 9.5P_{\text{rot}}$. The results from 26 snapshots with $0.0035 \leq t \leq 0.004$ of the simulation are superimposed in this graph. The top panel is for the northern hemisphere, the bottom panel is for the southern hemisphere.

angular momentum and partly sustain the internal differential rotation. It is very likely that the whole process of amplification and onset of the instability take much longer in reality than suggested by our initial-value simulations.

Instability occurs fairly early at an Alfvén angular velocity of about $\Omega_A = RB_\phi = 1000$. This is much smaller than the condition for stability, $\Omega^2 < \Omega_A^2$, derived by, e.g., Pitts & Tayler (1985). The difference is the much more complex structure of B_ϕ in our case with much stronger currents than the configuration used for the analytical study, where $B_\phi = s$, $B_z = \text{const.}$ The fraction of the critical Alfvén angular velocity to the actual rotation, Ω_A/Ω was even smaller in the stability analysis of the solar tachocline by Arlt, Sule & Rüdiger (2007) where the toroidal magnetic fields were even more localised.

Test runs on the linear stability (step II) indicate that a positive shear has a stronger stabilizing effect than negative shear in our particular configuration. The test was performed on the toroidal field at $t = 0.002$ from step I with $B_0 = 300$ and an arbitrary angular velocity $\Omega(s)$ increasing by 15 per cent from $s = 0$ to $s = 1$. The stability limit was at $S > 2$, while the stability limit for the same non-axisymmetric mode with $d\Omega/ds < 0$ was $S = 1.2$. This explains the steep increase of the lines of marginal stability in Fig. 2 after $t \sim 0.06$. In the pre-main-sequence evolution, it may be responsible for a long-term of stabilization as long as the star is gaining angular momentum on the surface by accretion. This situation is also stable against axisymmetric perturbations exciting the magnetorotational instability. It will be very interesting to combine the

simulations in this paper with the actual angular-momentum evolution obtained from combining the effects of accretion, magnetic star-disk coupling, and magnetized winds.

During most of the pre-main-sequence period, the star is rotating rather rapidly, with rotation periods of 1–2 days. Rapid rotation will suppress the Tayler instability in general. Once the accretion ceases and the disk turns into a more passive environment of the star, the stellar wind leads to a spin-down of the star. The increase of the rotation period can be quite steep, but only if strong magnetic fields are present (Stepień & Landstreet 2002). We are left with a contradiction here, since the spin-down requires poloidal fields, but the Tayler-instability providing these poloidal fields will set in only if the rotation period has already increased.

Another question concerns the time it takes for the unstable magnetic field to become visible on the surface. In the 3D simulation, we find a maximum of $B_{\text{max}}^{(\text{surf})} = 168$ at the surface, about 18 rotation periods after the onset of the instability. Note that the initial poloidal magnetic field was internal; the surface field was zero, but it develops surface fields of the order of $B_{\text{max}}^{(\text{surf})} \sim 10$ by diffusion. The bottom panel in Fig. 10 demonstrates that the motions arising from the instability are mostly horizontal. The emergence of the flux at the stellar surface is therefore rather a diffusive process. In the numerical simulation, the dynamical and diffusive time-scales are not as widely separated as in reality. We may argue that the emergence time is a diffusive one. Given a length-scale of say $0.1R_\odot$ for the rise and a microscopic diffusivity of $1000 \text{ cm}^2 \text{ s}^{-1}$, this time-scale results in about 9 Myr. The true rise time is certainly a combination of several effects and may be faster. The rise of a *stable* toroidal flux tube was studied by Mestel & Moss (2010). A tentative conversion of their time-scales into stellar values leads to 150 Myr and more which is more than an order of magnitude longer than in the unstable case (smaller structures).

The maximum poloidal field at the surface converts to about 2.7 kG using (6). The time-scale of 9 Myr is actually very interesting for Ap stars, it may take some time on the main sequence before the Ap phenomenon is observable (Hubrig, North & Mathys 2000). Other observations favour a persistence of magnetic fields from early Herbig Ae/Be stars to main-sequence Ap stars (Wade et al. 2007). By contrast, Hubrig et al. (2009) find decreasing magnetic fields in Herbig Ae/Be stars with age. While the observational picture will be gradually completing, simulations for a whole sequence of magnetic Reynolds numbers will be need to tell whether the emergence time-scale is indeed a fraction of the diffusion time. Note that the above mentioned 2.7 kG are small compared to the internally possible toroidal fields of 10^5 – 10^6 G. What appears to be a strong field in observations, can yet be a remnant of something much larger.

Also the amount of complexity of the surface magnetic fields is compatible with surface fields from Zeeman Doppler imaging (e.g. Kochukhov et al. 2004). Note that differences in initial conditions may cause a variety of final surface field strengths as well as a variety of emergence times, very similar to the complex observational picture that has been compiled up to now.

We are left with two possible ways to magnetic Ap stars: the existence of fossil field configurations that are stable for very long times on the one hand, and the emergence of magnetic fields by an instability on the other hand, where the ‘disrupted’ configuration is the observed and long-term stable one. Our paper studies the latter option. Since the differential rotation vanishes due to the presence of the fields, there is no further build-up of toroidal fields and the ‘disrupted’ fields will be fairly stationary over evolution-

ary time-scales. A comparison of the topology at very late stages with the ones obtained in compressible, but non-rotating simulations by Braithwaite & Nordlund (2006) will be interesting, once long enough simulations are available.

It is probable that the pre-main-sequence evolution of A stars is a mixture of various phenomena: the presence or absence of a substantial magnetic field in the collapsing cloud core, a possible short-lived dynamo during the convective phase (Arlt 2009), the angular-momentum evolution controlled by various torques, and the onset of the Tayler instability. It is still a challenge to explain why roughly 10 per cent of the possible scenarios lead to the Ap star phenomena, while the remaining fraction does not lead to strong fields at the stellar surfaces (fields may still be hidden in the star). However, the study of differences in the rotational evolution including differences in the amplitude of the differential rotation (delivering both a wide range of toroidal fields and large difference in stability limits) are a promising field to find discriminating situations between normal A stars and Ap stars.

Dynamo action – Apart from looking at the evolution of magnetic fields in the pre-main-sequence phase of Ap stars, we also studied the possibility of driving a dynamo from the instability in terms of representing it as a mean-field dynamo. We find enhanced values for the dynamo- α and related effects describing the field generation in a mean-field context. An axisymmetric dynamo driven by the Tayler instability cannot be excluded, although a proper energy source is missing in our setup. The prerequisite for the existence of an α -effect appears to be the presence of an inner boundary at which most of the α is concentrated, as is the kinetic helicity. The situation is thus interesting for Earth-like planetary interiors which have a solid inner core acting as an inner wall. To be interesting for a radiative zone, an inner boundary will be required such as a convective core, whose turbulent viscosity has a similar effect like a wall. This core should not be too far away from the Tayler-unstable zone, so a possible dynamo could be relevant for early B stars at best. The results do not support a dynamo from the Tayler instability in the solar tachocline though.

An interesting domain is the Earth's dynamo though, since the outer, fluid spherical shell of the core is very similar to what was studied here. Because of the rather small differential rotation of the core, the onset of current-driven instabilities as well as helicity distributions as shown in this Paper are possibly emerging in geodynamo simulations.

ACKNOWLEDGMENTS

The authors are grateful for the hospitality of NORDITA, Stockholm, where the idea of applying the test-field method to the Tayler problem materialized. We would also like to thank Svetlana Hubrig for helpful discussions.

REFERENCES

- Arlt R., Sule A., Rüdiger G., 2007, *A&A*, 461, 295
 Arlt R., 2009, in Strassmeier K. G., Kosovichev A. G., Beckman J. E., eds., *Proc. IAU Symp 259: Cosmic Magnetic Fields: From Planets, to Stars and Galaxies*. CUP, Cambridge, p. 443
 Braithwaite J., 2006a, *A&A*, 449, 451
 Braithwaite J., 2006b, *A&A*, 453, 687
 Braithwaite J., Nordlund Å., 2006, *A&A*, 450, 1077
 Brun A. S., Zahn J.-P., 2006, *A&A*, 457, 665
 Dikpati M., Cally P.S., Gilman P.A., 2004, *ApJ*, 610, 597
 Gellert M., Rüdiger G., Elstner D., 2008, *A&A*, 479, L33
 Giesecke A., Ziegler U., Rüdiger G., 2005, *Phys. Earth Planet. Int.*, 152, 90
 Gilman P. A., Fox P. A., 1997, *ApJ*, 484, 439
 Gough D. O., McIntyre M. E., 1998, *Nature*, 394, 755
 Hollerbach R., 2000, *Int. J. Num. Meth. Fluids*, 32, 773
 Hubrig S., North P., Mathys G., 2000, *ApJ*, 539, 352
 Hubrig S., et al., 2009, *A&A*, 502, 283
 Käpylä P. J., Korpi M. J., Brandenburg A., 2009, *A&A*, 500, 633
 Küker M., Rüdiger G., 2008, *J. Phys. Conf. Ser.* 118, 012029
 Kochukhov O., Bagnulo S., Wade G. A., Sangalli L., Piskunov N., Landstreet J. D., Petit P., Sigut T. A. A., 2004, *A&A*, 414, 613
 Mestel L., Moss D., 2010, *MNRAS*, 405, 1845
 Mikulašek Z., et al., 2008, *A&A*, 485, 585
 Pitts E., Tayler R. J., 1985, *MNRAS*, 216, 139
 Reshetnyak M. Yu., 2006, *Izvestiya, Phys. Solid Earth*, 42, 449
 Rüdiger G., Kitchatinov L. L., 1997, *Astr. Nachr.*, 318, 273
 Rüdiger G., Kitchatinov L. L., 2010, *Geophys. Astrophys. Fluid Dyn.*, 104, 273
 Schrunner M., Rädler K.-H., Schmitt D., Rheinhardt M., Christensen U. R., 2007, *Geophys. Astrophys. Fluid Dyn.*, 101, 81
 Spruit H., 1999, *A&A*, 349, 189
 Spruit H., 2002, *A&A*, 381, 923
 Stępień K., 2000, *A&A*, 353, 227
 Stępień K., Landstreet J. D., 2002, *A&A*, 384, 554
 Tayler R. J., 1973, *MNRAS*, 161, 365
 Vandakurov Yu. V., 1972, *SvA*, 16, 265
 Wade G. A., Bagnulo S., Drouin D., Landstreet J. D., Monin D., 2007, *MNRAS*, 376, 1145
 Watson M., 1981, *Geophys. Astrophys. Fluid Dyn.*, 16, 285
 Zahn J.-P., Brun A. S., Mathis S., 2007, *A&A*, 474, 145

This paper has been typeset from a $\text{\TeX}/\text{\LaTeX}$ file prepared by the author.